

TESS Data Release Notes: Sector 1, DR1

Michael M. Fausnaugh

*Kavli Institute for Astrophysics and Space Science, Massachusetts Institute of Technology,
Cambridge, Massachusetts*

Douglas A. Caldwell

SETI Institute, Mountain View, California

Jon M. Jenkins

Ames Research Center, Moffett Field, California

Jeffrey C. Smith, Joseph D. Twicken

SETI Institute, Mountain View, California

Roland Vanderspek

*Kavli Institute for Astrophysics and Space Science, Massachusetts Institute of Technology,
Cambridge, Massachusetts*

John P. Doty

Noqsi Aerospace Ltd, Billerica, Massachusetts

Jie Li

SETI Institute, Mountain View, California

Eric B. Ting

Ames Research Center, Moffett Field, California

Joel S. Villaseñor

*Kavli Institute for Astrophysics and Space Science, Massachusetts Institute of Technology,
Cambridge, Massachusetts*

December 5, 2018

Acknowledgements

These Data Release Notes provide information on the processing and export of data from the Transiting Exoplanet Survey Satellite (TESS, [Ricker et al., 2015](#)). The data products included in this data release are target pixel files, light curve files, collateral pixel files, full frame images (FFIs), cotrending basis vectors (CBVs), and Data Validation (DV) reports, time series, and associated xml files.

These data products were generated by the TESS Science Processing Operations Center (SPOC [Jenkins et al., 2016](#)) at NASA Ames Research Center from data collected by the TESS instrument, which is managed by the TESS Payload Operations Center (POC) at Massachusetts Institute of Technology (MIT). The format and content of these data products are documented in the [Science Data Product Description Document \(SDPDD\)](#)¹. The SPOC science algorithms are based heavily on those of the Kepler Mission science pipeline, and are described in the Kepler Data Processing Handbook ([Jenkins, 2017](#)).² The Data Validation algorithms are documented in [Twicken et al. \(2018\)](#) and [Li et al. \(2018\)](#). The TESS Instrument Handbook ([Vanderspek et al., 2016](#)) contains more information about the TESS instrument design, detector layout, data properties, and mission operations.

The TESS Mission is funded by NASA's Science Mission Directorate.

This report is available in electronic form at
<http://https://archive.stsci.edu/tess/>

¹<https://archive.stsci.edu/missions/tess/doc/EXP-TESS-ARC-ICD-TM-0014.pdf>

²<https://archive.stsci.edu/kepler/manuals/KSCI-19081-002-KDPH.pdf>

1 Observations

TESS Sector 1 observations include physical orbits 9 and 10 of the spacecraft around the Earth. Data were collected over a 27.9-day period with a 1.13 day pause during perigee passage while downloading data.

Table 1: Sector 1 Observation times

	UTC	TJD ^a	Cadence #
Orbit 9 start	2018-07-25 19:00:27	1325.29278	70444
Orbit 9 end	2018-08-08 00:29:51	1338.52153	79968
Orbit 10 start	2018-08-09 03:39:19	1339.65310	80782
Orbit 10 end	2018-08-22 16:14:51	1353.17778	90519

^a TJD = TESS JD = JD - 2,457,000.0

The spacecraft was pointing at RA (J2000): 352.6844°; Dec (J2000): -64.8531°; Roll (deg): -137.8468. Two-minute cadence data were collected for 15,898 stars and full-frame images were collected every 30 minutes. The two-minute cadences consist of 48 co-adds of 2 second exposures and the FFI cadences consist of 720 co-adds of 2 second exposures. Details of the data collection and on-board cosmic ray mitigation can be found in the instrument handbook. See the TESS project [Sector 1 observation page](https://tess.mit.edu/observations/sector-1)³ for the coordinates of the spacecraft pointing and center field-of-view of each camera, as well as the detailed target list. Fields-of-view for each camera showing the two-minute targets can be found at the TESS Guest Investigator Office [observations status page](https://heasarc.gsfc.nasa.gov/docs/tess/status.html)⁴. Figure 1 shows an ecliptic projection of the FOV for Sector 1 observations.

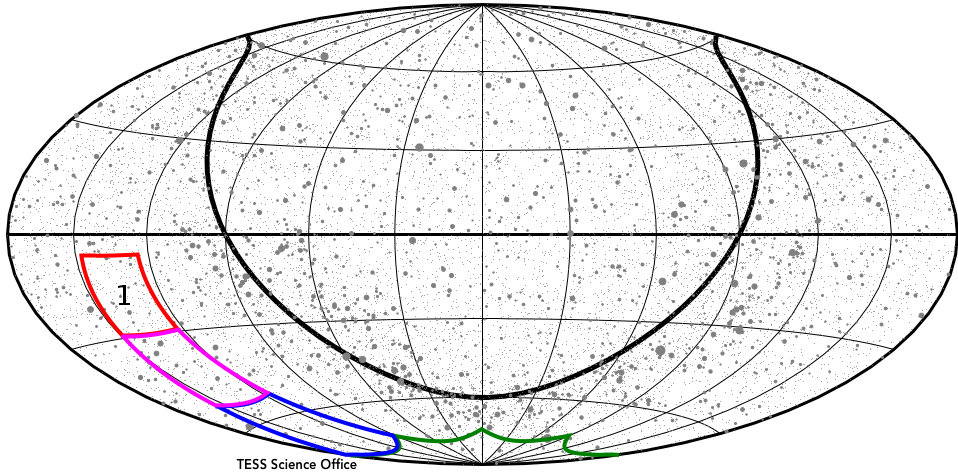


Figure 1: Projection of the TESS field of view onto the celestial sphere for Sector 1 in ecliptic coordinates. The fields of view of Cameras 1, 2, 3, 4 are shown in red, magenta, blue, and green, respectively.

³<https://tess.mit.edu/observations/sector-1>

⁴<https://heasarc.gsfc.nasa.gov/docs/tess/status.html>

1.1 Notes on Individual Targets

Four very bright stars ($\text{Tmag} \lesssim 2$) with large pixel stamps were not processed in the photometric pipeline. Target pixel files with raw data are provided, but no light curves were produced. The affected TIC IDs are 44577667, 238196512, 394046358, and 38877693.

Five targets were erroneously placed on the wrong CCD in Camera 4. A target pixel file for each target is provided, although the raw pixel data does not contain the target designated in the file names. No optimal apertures or light curves were produced. The affected TIC IDs are 149251611, 220478335, 149542119, 300160320, and 176954932.

Two targets (253923637 and 300015238) have very bright stars nearby (253923638 and 300015239, respectively). The contaminating flux for these objects is very large and the pipeline assigns them disjoint photometric apertures, which likely causes uncorrected systematic errors in the light curves.

One target (197641601) had a pixel stamp selected (25x25 pixels) that did not fully capture the bleed trails.

Four targets (281592043, 419793478, 469844770, and 469849622), near the corners of Camera 2, are off-center in their pixel stamps. This was due to an error in the focal plane geometry model that was corrected for future sectors. As a consequence, the optimal apertures are clipped by the edge of the stamps. Other targets in the corners of Camera 2 may also be slightly off-center; however, all other pixel stamps fully contain the optimal aperture.

1.2 Spacecraft Pointing

During Sector 1 observations the reaction wheel speeds were reset to low values every 2.5 days to improve pointing precision. Each maneuver uses the thrusters to remove angular momentum from the reaction wheels. These so-called “momentum dump” take approximately 5 minutes, during which time the spacecraft is not in Fine Pointing mode, and result in degraded pointing stability. After completing each momentum dump maneuver the spacecraft returns to Fine Pointing mode and nominal pointing stability returns after \sim 10 minutes.

Cadences collected during these intervals have data quality flags with bit 6 set (Reaction Wheel Desaturation Event) and bit 8 set (Manual Exclude)—see §2 below. The quality flag intervals include a \sim 20 minute buffer for the fine pointing mode to resume.

In addition, the time between approximately 2018-08-16 16:00 UTC and 2018-08-18 16:00 UTC (TJD 1347–1349) exhibited anomalously high pointing jitter, due to an improperly configured Fine Pointing mode calibration. The variable pointing behavior is a dominant systematic effect in the light curves that can only partially be corrected by cotrending, so a large fraction of these cadences are manually excluded with quality flags (see §2 and §4.1).

Figure 2 summarizes the pointing performance over the course of the sector based on Fine Pointing telemetry. The sudden decreases in dispersion mark the momentum dumps, while the large jitter towards the end of the sector marks the period with an incorrectly configured Fine Pointing calibration.

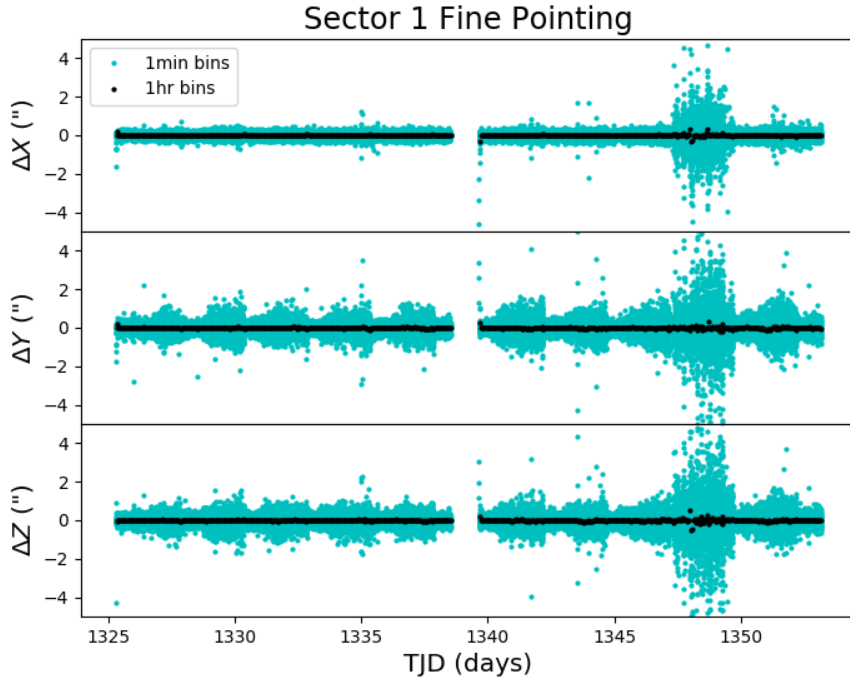


Figure 2: Guiding corrections based on spacecraft fine pointing telemetry. The delta-quaternions from each camera have been converted to spacecraft frame, binned to 1 minute and 1 hour, and averaged across cameras. Long-term trends (such as those caused by differential velocity aberration) have also been removed. The $\Delta X/\Delta Y$ directions represent offsets along the detectors' rows/columns, while the ΔZ direction represents spacecraft roll. The sudden decrease in the dispersion every 2.5 days marks the momentum dumps. The large jitter towards the end of the sector marks the period with an incorrectly configured fine pointing calibration.

1.3 Scattered Light

Figure 3 shows the median value of the background estimate for all targets on a given CCD as a function of time. The changes are caused by scattered light from the Earth and Moon that varies with the Earth/Moon distance, azimuth, and elevation during the spacecraft's orbit.

When the Earth/Moon rises above the sun shade, low-level patchy scattered light features appear in the images. This causes the enhanced background level in the first two-thirds of each orbit in Figure 3. When the Earth/Moon moves within 37° of a camera's boresight, scattered light patterns and complicated features such as glints may appear. To help identify observing periods affected by scattered light, Figure 4 shows the angle between the Earth/Moon and each camera's boresight as a function of time.

Although local background subtraction generally removes the effects of scattered light, the illumination can change very rapidly over a two minute cadence (for example, near perigee or at low Earth/Moon angles relative to the camera boresights). The main scattered

light features to be aware of in Sector 1 are as follows:

1. There is an oscillation in the background with a period of 1 day caused by the rotation of the Earth.
2. The Moon gets quite close to the FOV of Camera 1 at the end of the sector. On the last day of observations, the angle between the Moon and the boresight of Camera 1 is $<30^\circ$, which causes of the large spike in the upper left panel of Figure 3.

More detail about stray light can be found in the Instrument Handbook.

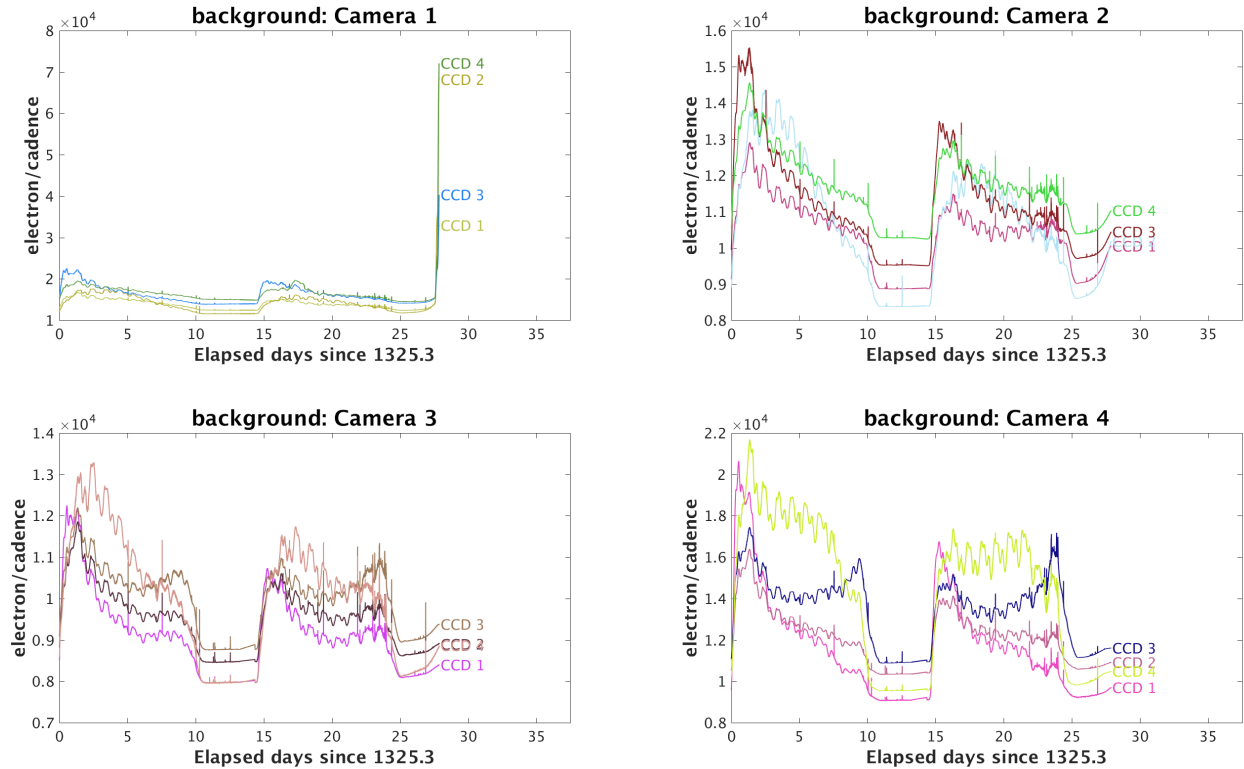


Figure 3: Median background flux across all targets on a given CCD in each camera. The changes are caused by variations in the orientation and distance of the Earth and Moon. The oscillating feature has a 1-day period and is caused by the rotation of the Earth. The large spike at the end of the sector in Camera 1 is caused by the Moon moving within 30° of the camera boresight.

2 Data Quality Flags

See the SDPDD (§9) for a list of data quality flags and the associated binary values used for TESS data, and the instrument handbook for a more detailed description of each flag.

The following flags were not used in Sector 1: bits 1, 2, 7, 9, 11, and 12 (Attitude Tweak, Safe Mode, Cosmic Ray in Aperture, Discontinuity, Cosmic Ray in Collateral Pixel, and

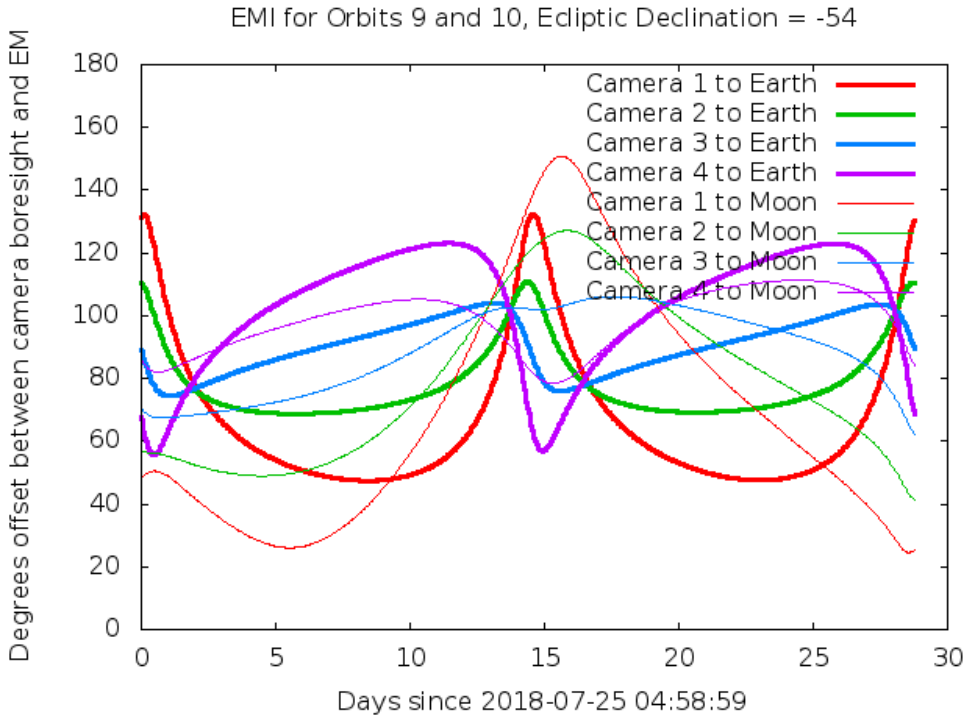


Figure 4: Angle between the four camera boresights and the Earth/Moon as a function of time. When the Earth/Moon moves within 37° of a camera’s boresight, scattered light patterns and complicated features such as glints may appear. At larger angles, low level patchy features may appear. This figure can be used to identify periods affected by scattered light and the relative contributions of the Earth and Moon to the background. However, the background intensity and locations of scattered light features depend on additional factors, such as the Earth/Moon azimuth and distance from the spacecraft.

Straylight). Bits 7, 9, and 11 are unlikely to ever be applicable to TESS data (see the instrument handbook).

Cadences marked with bits 3, 4, and 6 (Coarse Point, Earth Point, and Reaction Wheel Desaturation Event) were marked based on spacecraft telemetry.

Cadences marked with bit 5 and 10 (Argabrightening Events and Impulsive Outlier) were identified by SPOC pipeline results. Bit 5 marks a sudden change in the background measurements. In practice, all bit 5 flags are caused by the unstable pointing at times near momentum dumps—this flag may be revised in future sectors (see the instrument handbook). Bit 10 marks an outlier identified by PDC and omitted from the cotrending procedure.

Cadences marked with bit 8 (Manual Exclude) are ignored by PDC, TPS, and DV for cotrending and transit searches. These cadences were identified with the following procedure:

Using spacecraft telemetry from the fine pointing system, we first identified all cadences with pointing excursions either >10 arcseconds (0.5 pixels) or >5 times the standard deviation of the pointing offset time series. These cadences were excluded in an initial run of the pipeline, and the resulting light curves were corrected for systematic errors using PDC. We then calculated the median absolute deviation (MAD) of the normalized light curves at

each cadence for a collection of quiet stars with average variations $<1\%$ after cotrending. Cadences with MAD PDC flux values greater than 1×10^{-3} were then excluded from the final run of the pipeline—see Figure 5 for an illustration. This procedure predominantly flags cadences during the two day period of poor performance, as well as a subset of cadences just before and during each momentum dump.

FFIs were only marked with bit 6 (Reaction Wheel Desaturation Events). Only one or two FFIs are affected by each momentum dump.

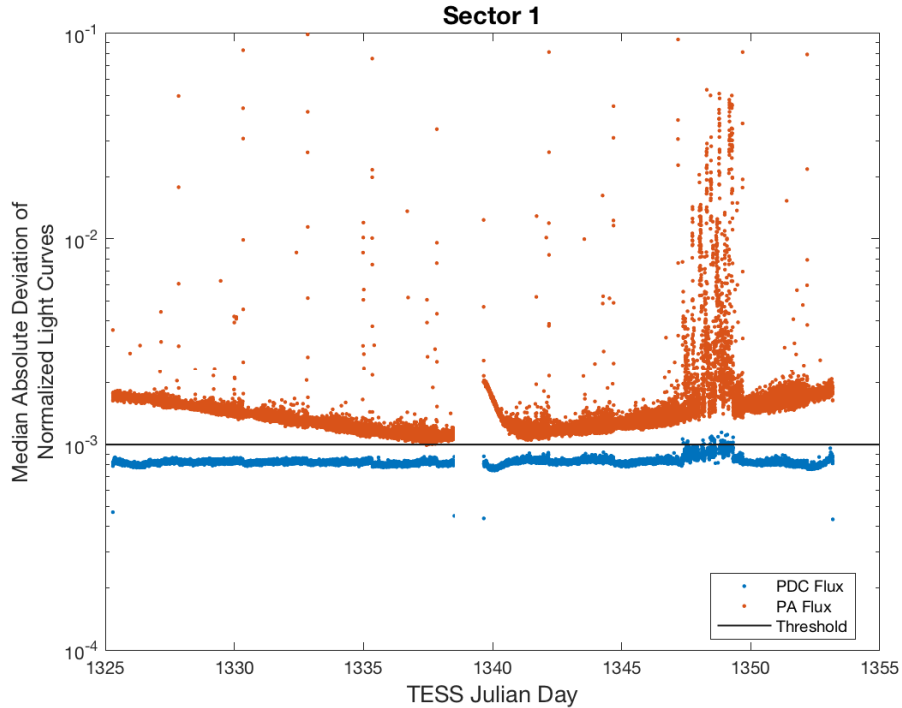


Figure 5: Median absolute deviation (MAD) for the 2-minute cadence data from Sector 1, showing the performance of the cotrending after identifying Manual Exclude data quality flags. The MAD is calculated in each cadence across stars with flux variations less than 1% for both the PA (red) and PDC (blue) light curves, where each light curve is normalized by its median flux value. The scatter in the PA light curves is much higher than that for the PDC light curves, and the outliers in the PA light curves are largely absent from the PDC light curves due to the use of the anomaly flags. Note that the MAD for some of the cadences in the PDC light curves have values slightly above 1×10^{-3} threshold after reprocessing. Note also that the first and last cadences in each orbit are treated as gaps by PDC.

3 Anomalous Effects

3.1 Mars

Mars was near opposition during Sector 1 and landed in the field-of-view of Camera 1 for ~ 2 days at the beginning of observations. Specifically, it is in Camera 1, CCD 4, output channel D, and visual inspection of the FFIs and target pixel files shows an extremely bright object with excess charge spread across the pixels in this output channel.

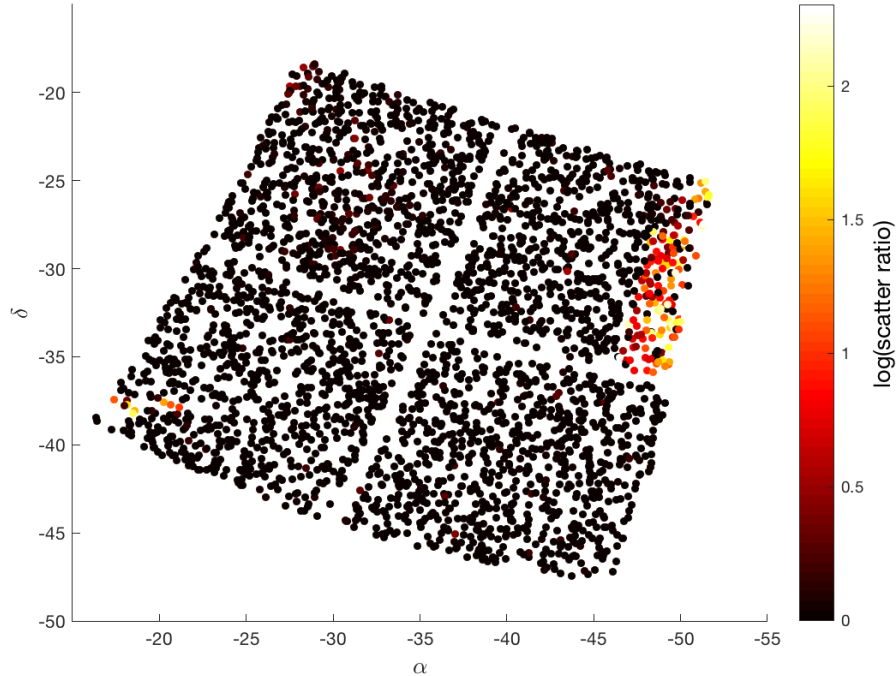


Figure 6: Ratio of the scatter in the first two days (520 cadences) of the PDC light curves to that of the rest of the time series for each target in Camera 1 in celestial coordinates. For display purposes, the ratio has been limited to the interval [1,10]. Stars with elevated scatter in the first two days are likely to have been affected by scattered light from Mars (CCD 4) and its reflection (CCD 2). Clockwise starting with the bottom right, the CCD numbers are 1, 2, 3, 4.

As a consequence, photometry is unreliable in this section of the CCD in the first ~ 510 cadences of the sector. The presence of Mars has three other important effects:

1. Because of the unreliable flux, pixels and light curves often have wildly fluctuating values during this period, as shown in Figure 6.
2. Cotrending basis vectors (CBVs) are calculated per CCD, and targets affected by Mars on channel D make small contributions to the CBVs for Camera 1, CCD 4. This manifests as a step function and increased dispersion for the first 2 days in several of the CBVs. Although the CBVs are able to correct light curves for targets on channel

D in several cases, they sometimes also contaminated the light curves for targets on other parts of the CCD (output channels A, B, and C). The total number of affected targets is \sim 240 (out of 3208 targets), and the effect is easy to identify by the decreased scatter after the first two days of the sector.

3. An internal reflection causes light from Mars to appear on the opposite corner of the camera (CCD 2). The effect is much weaker, but some targets display additional scatter in their light curves during the first two days of observations (Figure 6).

3.2 Smear Correction Issues

In some cases, excess charge can appear in the smear rows (rows 2049–2058) of a given column, which results in an over-subtracted smear correction along that column. There are two general causes:

1. **Bright source bleed near the edge of a CCD:** A bright source near the bottom of the CCD can bleed into the frame store, which will add charge to the previous cadence as it is readout. In these cases, bleed trails will be evident in the virtual and smear rows of the CCD frame. Because there are 10 buffer rows below the CCD imaging region, some bright sources can still affect the lower frame store even if they are not directly imaged. This appears to be the case for Canopus (Alpha Carinae) in Sector 1—see the diffuse glow at the bottom of Camera 4, CCD 4, output channel C, and the bleed trails in the top virtual/smear rows of column 1267–1270.

If the source is near the top of the CCD, the charge can bleed into the charge injection region and bloom horizontally (across columns)—however, this effect is not present in Sector 1.

2. **Charge Traps** Charge traps can change the distribution of charge along a column during readout, and generally move charge from stars near the top of the frame into the smear rows. A charge trap in the frame store will also deposit charge in the virtual rows. These columns display a weak gradient in rows 2059–2068 (or 2078 for traps in the frame store). The charge traps appear to be stable in time, and a full list of affected columns can be found in the instrument handbook.

3.3 Black Flutter

Black flutter is an anomalous oscillation in the overclock column levels, and was observed in Camera 4, CCD 2 between (approximately) cadences 82600 and 83700. The oscillation appears as high frequency noise modulated by a 50 minute envelope, and is visually similar to a wave train. The individual wave packets do not show a coherent frequency—see the instrument handbook for more details. The root cause of this behavior has not been identified, but standard calibration procedures remove its effect.

3.4 Fireflies and Fireworks

Table 2 lists all firefly and fireworks events for Sector 1. These phenomena are small, spatially extended, comet-like features in the images that may appear one or two at a time (fireflies) or in large groups (fireworks). These features are caused by foreground dust particles moving quickly through the field of view, likely originating from meteoroid impacts. These features were identified in commissioning and characterized with a number of experiments. See the instrument handbook for a complete description.

Table 2: Sector 1 Fireflies and Fireworks

FIN Start	FIN End	FFI Start	FFI End	Cameras	Description
4717	4718	2018207052942	2018207055942	2, 3, 4	single long firefly
4776	4777	2018208105942	2018208112942	3	single firefly
5189	5190	2018217012942	2018217015942	1, 2, 3, 4	fireworks
5225	5226	2018217192942	2018217195942	3, 4	3 fireflies
5238	5239	2018218015942	2018218022942	2	2 fireflies
5405	5406	2018221132941	2018221135941	3	single firefly
5416	5418	2018221185941	2018221195941	2	2 fireflies
5426	5427	2018221235941	2018222002941	2	single firefly
5505	5506	2018223152941	2018223155941	3	single firefly

3.5 Undershoot

Undershoot is an analog electronic effect whereby the digitized CCD output is a weighted sum of the current pixel value and previous values (Vanderspek et al., 2016; Van Cleve & Caldwell, 2016). Details on the nature and amplitude of the undershoot can be found in the instrument handbook. Figure 7 shows a zoomed portion of an FFI that contains a very bright, saturated and bleeding star. This image has been clipped to accentuate the undershoot affect, which is $\sim 0.15\%$ of the previous pixel's value, as estimated from the bleeding vertical trail of the central star in this image. The undershoot for TESS is small and can be ignored for most analysis purposes.

3.6 Video Crosstalk

Video crosstalk is a phenomena whereby the electronic signals from adjacent CCD readout electronics circuits can be superimposed on each other (Vanderspek et al., 2016; Van Cleve & Caldwell, 2016). Since this is an electronic effect, the contamination can be either negative or positive. Figure 7 contains several negatively cross-talked star images from a neighboring CCD readout channel. See the instrument handbook for details on the prevalence and levels of video crosstalk.

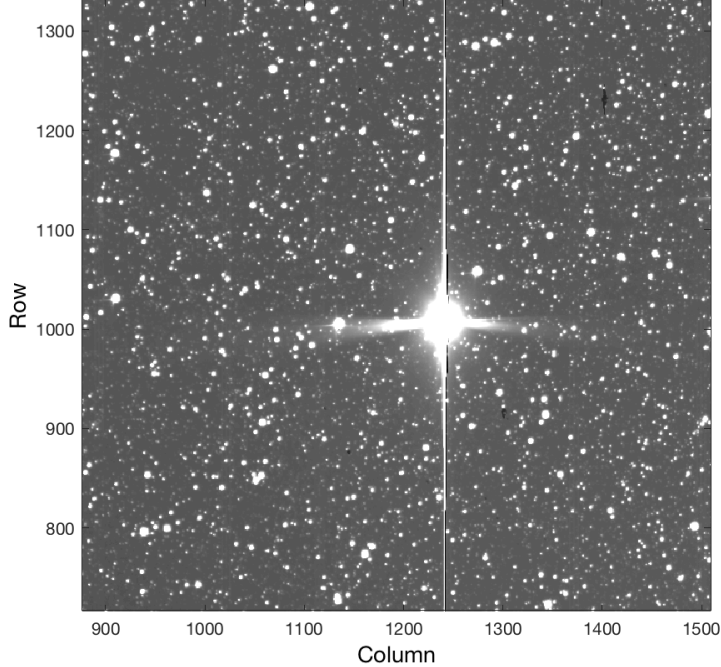


Figure 7: Zoom of an FFI for Camera 2, CCD 3 (tess2018226155942-s0001-2-3-0120-s_ffic.fits). This image has been clipped to accentuate small amplitude features. The columns to the right of the bleeding charge from the bright star display the undershoot effect, and have slightly negative values in the calibrated image. Video crosstalk, evident as negative (black) images of stars on adjacent readout amplifiers, can be seen at various locations (e.g., at row 1234, column 1402).

3.7 Asteroids

Asteroids with high proper motion pass through a subset of the target stamps and contribute a variable amount of light as they move through the target apertures, which is evident in the light curves as short- to medium-duration “bumps.” In some cases they also cause overestimation in the local background, resulting in flux values that go below the baseline flux value for the star. This happens most frequently in Camera 1, which is nearest the ecliptic. See TIC ID 99769182 for a representative example.

3.8 Reference Flux

The pipeline used a pre-flight flux calibration estimate of 12,500 counts per second for a 10th magnitude star to compute the photometric apertures for the two-minute cadence targets. The on-sky performance is about 20% better, close to 15,000 counts per second. This may have a small impact on the optimal apertures. The reference flux was updated for Sector 2 processing.

3.9 1-D Black Correction

The 1-D black correction (also known as “bias correction”) attempts to correct for variations in both time and row in the black level (“bias” level) of the CCD readouts. This correction is a polynomial fit across rows in the overclock regions of each CCD output channel. The current correction is fit to the average of all 11 columns for each CCD channel. However, residual effects from the imaging pixels influence the first one or two columns. This is a small effect in cases where it is present, but future versions of the calibration module will ignore these columns for the 1-D black correction.

In addition, the order of the polynomial fit was selected using an Akaike Information Criterion, but was observed to vary between 0 and 6 for different cadences. Although we have not found an individual case where the order makes a substantial difference (the correction is nearly constant along rows), we plan to force a uniform fit order for future data sets.

3.10 Timing Precision and Accuracy

Due to an error in the spacecraft clock kernel, the two-minute cadence durations vary by ~ 0.51 msec and the FFI durations vary by ~ 7.8 msec. The changes in the durations are discontinuous and occur at reference points used to interpolate the conversion from space-craft time to TJD. However, these errors are well within TESS’s 1 second timing accuracy requirement. Future sectors do not have this problem, and the Sector 1 data is likely to be reprocessed with an improved clock kernel in the future.

4 Pipeline Performance and Results

4.1 Light Curves

Light curves are generated for the two-minute cadence targets using simple aperture photometry (SAP_FLUX, [Morris et al., 2017](#)). The flux values consist of the sum of the pixels in an aperture that optimizes the signal-to-noise for the target ([Bryson et al., 2017](#)). The SAP light curves are background corrected using a local background level determined from the trimmed mean of a set of background pixels. In each target pixel file, there is an aperture mask image extension that identifies the optimal aperture pixels and the background pixels by setting bits 2 and 3, respectively. Flux-weighted centroids are also reported for each target, with pixel response function (PRF) centroids fitted to a subset of targets. Uncertainty estimates are provided with each quantity reported in the light curve and target pixel files.

4.1.1 Systematic Error Removal

Simple aperture photometry light curves retain significant common-mode systematics as a result of focus changes, spacecraft pointing jitter, long-term pointing drifts due to differential velocity aberration, and other stochastic errors (such as attitude tweaks, safe modes, etc.). The Presearch Data Conditioning (PDC) pipeline module uses singular value decomposition (SVD) to identify time-correlated instrumental signatures in the light curves. The resulting

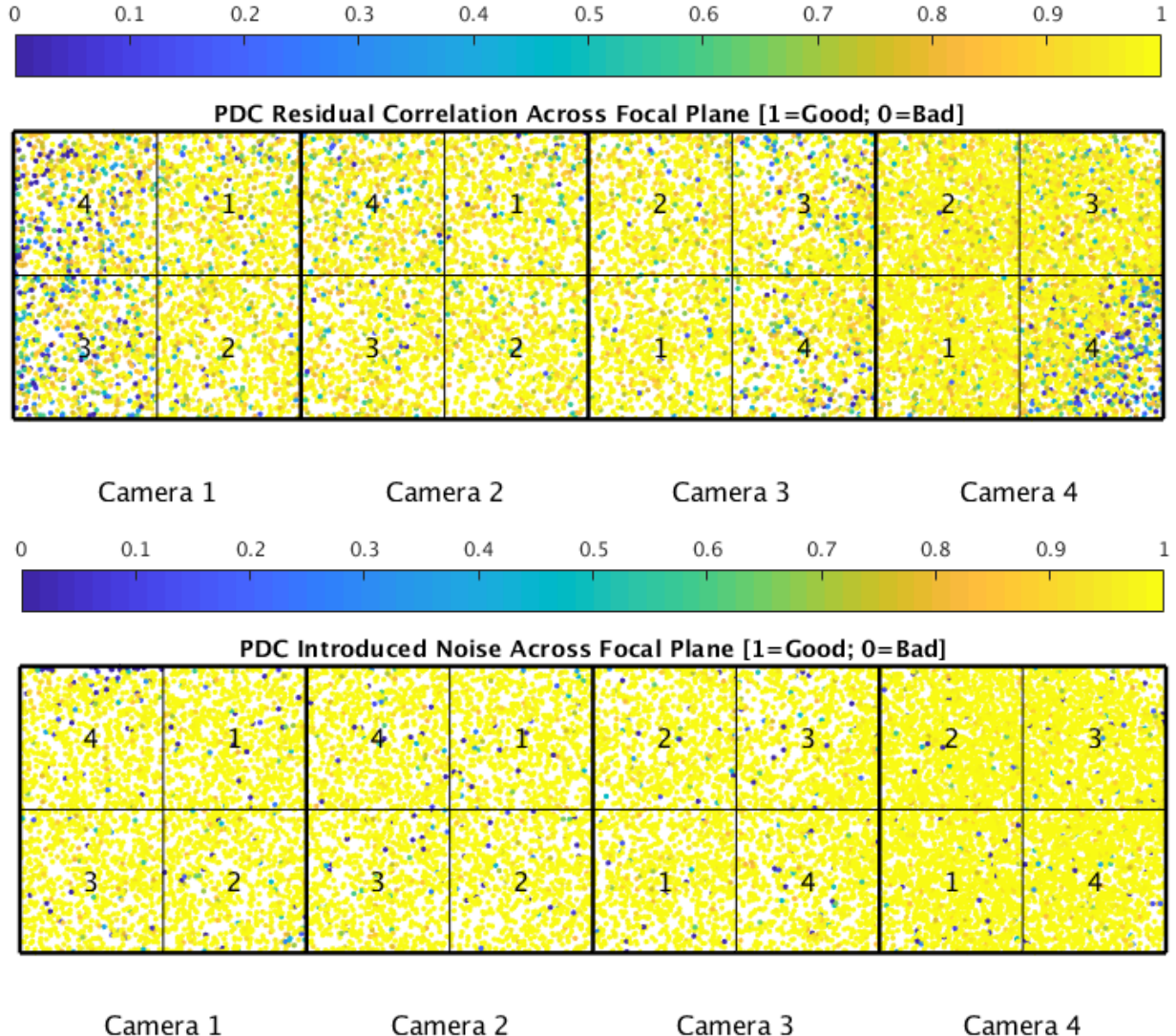


Figure 8: PDC residual correlation goodness metric (top panel) and PDC introduced noise goodness metric (bottom panel). The metric values are shown on a focal plane map indicating the camera and CCD location of each target. See §4.1.1 for more details.

co-trending basis vectors are projected out of each stellar light curve using a Bayesian maximum a posteriori (MAP) approach, which constrains the fit coefficients to reasonable values based on empirical prior and posterior distributions. Additionally, PDC corrects the flux for each target to account for crowding from other stars and flux in the PRF wings missing from the optimal aperture (CROWDSAP and FLFRSAP, respectively in the light curve file).

PDC has two modes of operation: Single-Scale (ssMAP, [Smith et al., 2012](#)) and Multi-Scale (msMAP , [Stumpe et al., 2014](#)). Generally speaking, msMAP is better at preserving and cleaning light curves at transit time scales, and ssMAP is better at preserving long period signals. After both MAP methods are applied, two figures of merit are calculated for each light curve: 1) Residual Correlation and 2) Introduced Noise. The method that removes

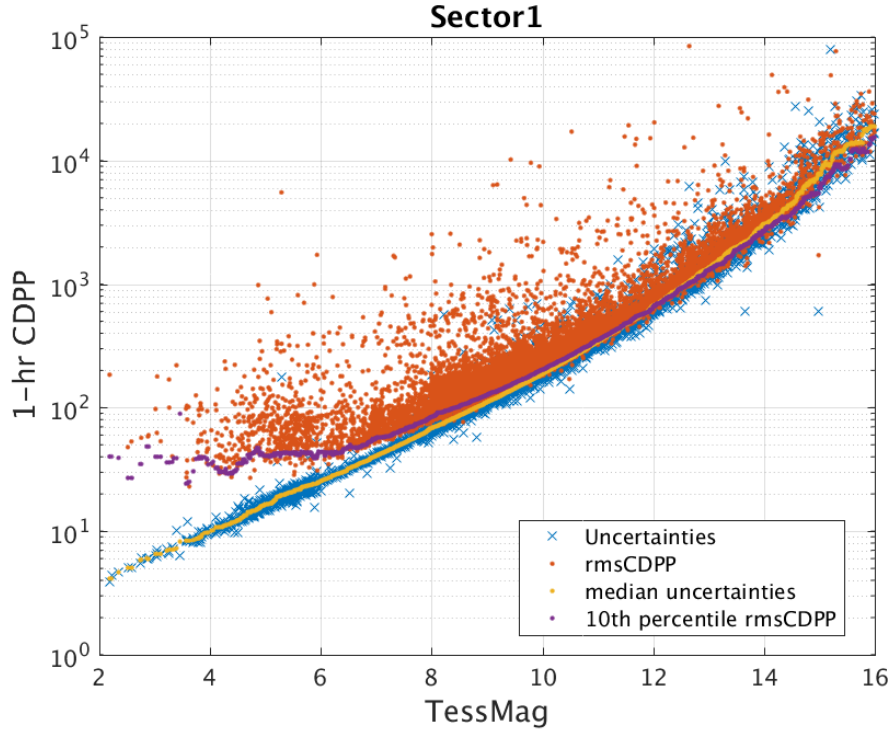


Figure 9: 1-hour CDPP. The red points are the RMS CDPP measurements for the 15,889 light curves from Sector 1 plotted as a function of TESS magnitude. The blue x's are the uncertainties, scaled to 1-hour timescale. The purple curve is a moving 10th percentile of the RMS CDPP measurements, and the gold curve is a moving median of the 1-hr uncertainties.

the most correlation between light curves (i.e., no remaining systematics) while minimizing any introduced noise (i.e., does not overfit the CBVs) is chosen for the correction, and listed in the binary table header of each light curve file.

Figure 8 gives the PDC goodness metrics for residual correlation and introduced noise on a scale between 0 (bad) and 1 (good). The correlation goodness metric is calibrated such that a value of 0.8 means there is less than 10% mean absolute correlation between the target under study and all other targets on the CCD. The introduced noise metric is calibrated such that a value of 0.8 means the power in broad-band introduced noise is only slightly above the level of uncertainties in the flux values. It is immediately apparent that performance is generally good and quite uniform over most of the field of view. Some residual correlation exists at the outer peripheries of Camera 1 and 4. In general, higher motion and jitter regions of the field of view experience worse residual correlation. Regions of the sky with high crowding, such as within the Galactic plane, can also experience worse introduced noise.

The PDC goodness metrics were not calibrated until Sector 3 processing. The metrics reported in the figures here are properly calibrated, but the values reported in the light curve FITs files are not reliable. The calibrated goodness metrics are available as a supplementary data file with these release notes.

The edges of the time series are the most troublesome to PDC, and one can find examples

of edge effects in light curves. If a signal is present near the beginning or end of the time series then one should retain some caution towards its validity. Comparison of the SAP_FLUX time series with the PDCSAP_FLUX time series can help resolve the question of whether a feature at the edge of the data set was erroneously introduced by PDC or is likely to be a real astrophysical effect. Another period with sub-optimal performance is during the poor pointing time between approximately 2018-08-16 16:00 UTC and 2018-08-18 16:00 UTC (TJD 1347–1349). Although PDC does an excellent job of correcting the systematics during this time, the large errors cannot be perfectly removed.

4.1.2 Photometric Precision

Figure 9 shows the achieved Combined Differential Photometric Precision (CDPP) at 1-hour timescales for all targets (Jenkins et al., 2010; Christiansen et al., 2012). The photometric uncertainties are dominated by pointing jitter, but the best light curves are well below the mission requirements of (1) a systematic error floor at 60 ppm and (2) achieved CDPP at 10th magnitude of 230 ppm. The RMS CDPP measured at 0.5, 1.0, and 2.0 hours is reported in the light curve and target pixel files for each target.

4.1.3 Negative Flux

At some epochs, the light curves and/or some pixels in the target pixel files have negative flux. We have identified two causes:

1. As mentioned in §3.1, the presence of Mars in Camera 1, CCD 4 affects the cotrending basis vectors. The final PDC light curves are also corrected for crowding in the photometric aperture, and the combination of these effects can result in highly fluctuating light curve values that can include negative points.
2. During momentum dumps, the targets can move significantly within, or entirely outside of, their apertures. This often leads to negative pixels and/or light curve values after background subtraction. These epochs are always flagged with bit 8 (Manual Exclude) and are not included in further analysis.

Once the momentum dumps and the large pointing excursions (>10 arcsec) are excluded, only 48 of the PDC light curves have any negative points, with the majority caused by Mars.

4.2 Transiting Planet Search

In Sector 1, 15,889 targets were subjected to a search for transiting planet signatures in the Transiting Planet Search (TPS) module of the SPOC Pipeline.

The TESS SPOC Pipeline is based closely on the *Kepler* Science Data Processing Pipeline. The final Kepler Pipeline transit search and data validation results (DR25) are described at length in Twicken et al. (2016). Significant differences between the final *Kepler* transit search and the TESS Sector 1 transit search are as follows:

1. The TESS light curve cadence is 2 minutes whereas the *Kepler* (long) cadence employed in the transit search was 30 minutes.

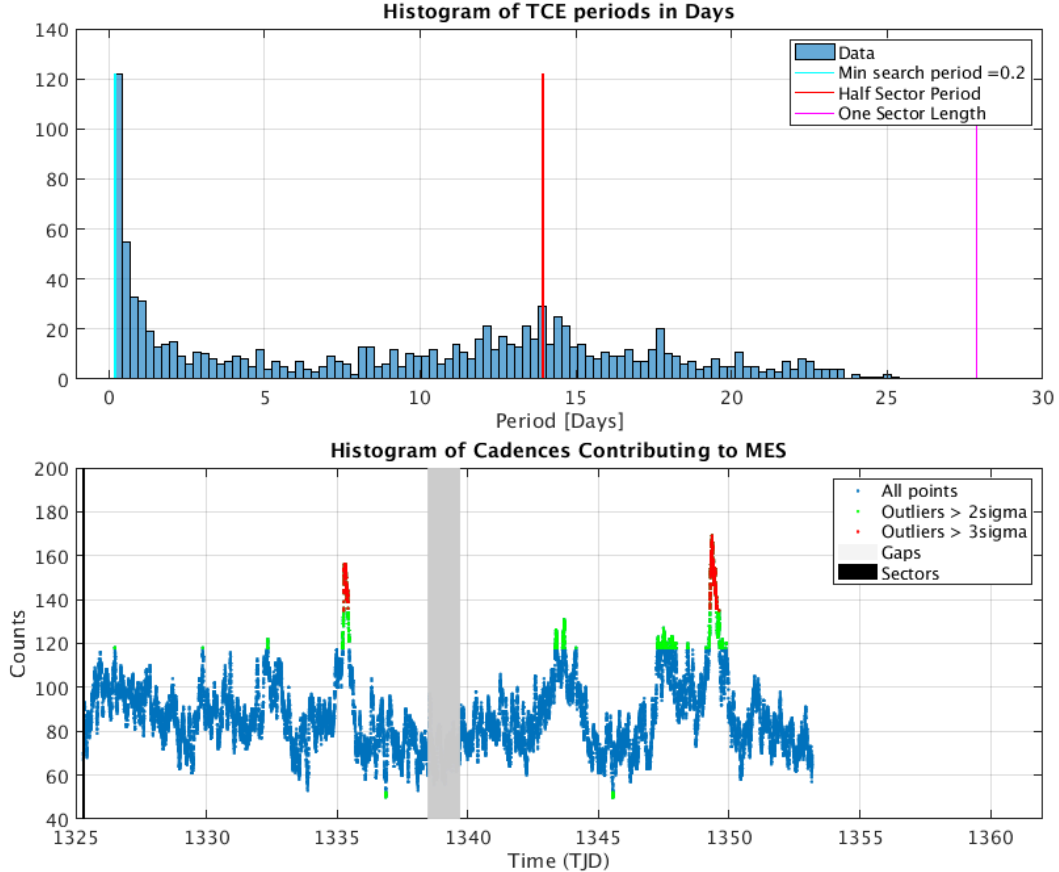


Figure 10: Top: Histogram of orbital periods for 1032 TCEs produced in the TPS transit search. TCEs represent the strongest transit signals found across all search durations by targets that exceed the 7.1σ detection threshold and survive all transit consistency checks as described in [Twicken et al. \(2016\)](#). Bottom: Number of TCEs which are in-transit on each cadence in the observing sector. Narrow peaks representing cadences with 2σ and 3σ excesses of TCEs are highlighted in green and red respectively. Isolated peaks are caused by a single event in the spacecraft/instrument and result in spurious TCEs.

2. TESS TCEs require two transits only whereas *Kepler* TCEs required three. The allowance of two transit TCEs for TESS increases the period for which transiting planets may be detected with the cost of additional false positives.
3. The minimum transit search period for TESS is 0.2 days whereas the minimum *Kepler* search period was 0.5 days.
4. The fifteen trial transit pulse durations employed in the TESS transit search (0.5, 1.0, 1.5, 2.0, 2.5, 3.0, 3.5, 4.5, 5.0, 6.0, 7.5, 9.0, 10.5, 12.5, and 15 hr) differ from those used in the *Kepler* Pipeline.
5. Identification and removal of harmonic content in light curves is disabled for the Sector 1 TESS transit search. Removal of harmonic content for *Kepler* increased the

sensitivity to planets on host stars with modulated light curves at the expense of degradation of some short-period transit signatures.

A histogram of the orbital periods for the Sector 1 TPS TCEs is shown in the top panel of Figure 10. The orbital periods extend to nearly the full length of the observing sector because of the two-transit requirement. The count of orbital periods decreases with period for the shortest-period TCEs as expected. There is an excess of TCEs at mid to long orbital periods that is non-physical. The bulk of these TCEs are due to false alarms driven by pointing excursions, momentum dumps, and scattered light. Narrow peaks in the histogram are likely due to false positives associated directly with momentum dumps that occurred at 2.5 day intervals in each of the two orbits of Sector 1.

The bottom panel of Figure 10 shows the number of TCEs at a given cadence that exhibit a transit signal. Narrow peaks with 2 and 3σ excesses of TCEs are colored in green and red respectively, which suggest “preferred” cadences in the ensemble of TCE detections. These peaks are caused by a single event on the spacecraft and result in spurious TCEs. An attempt was made to exclude cadences associated with the 2.5 day momentum dumps and other pointing excursions from the transit search as described in §2; however these events still trigger many false positives in the transit search.

4.3 Data Validation

The 1032 targets that produced TCEs in TPS were then processed in the Data Validation (DV) Pipeline module. TCEs are characterized in DV with transiting planet model fits, light curves are iteratively searched for additional TCEs after modeled transit signatures are removed, and a suite of diagnostic tests is performed to help distinguish between genuine transiting planets and false positive detections.

The *Kepler* DV architecture, diagnostic tests, and archive products are described in detail by [Twicken et al. \(2018\)](#), and the transit model fitting is documented in [Li et al. \(2018\)](#). DV produces DV Reports (PDF), Results files (XML), and Time Series files (FITS) by target, and one-page Report Summaries by TCE (PDF). Major differences between the TESS Sector 1 and *Kepler* DR25 DV runs are as follows:

1. The maximum number of TCEs permitted per TESS DV target is six compared with 10 for *Kepler*.
2. The quadrature error term for TESS difference imaging and offset analysis is 2.5 arcsec whereas the quadrature error term for *Kepler* was 0.0667 arcsec. This implies that TESS centroid offsets < 7.5 arcsec cannot be significant at the 3σ level.
3. *Kepler* TCEs were matched against ephemerides of known Kepler Objects of Interest (KOIs) at the time that DV was run, but TESS TCEs are not yet matched against ephemerides of TESS Objects of Interest (TOIs) or confirmed transiting planets in the TESS fields of view.
4. The centroid motion diagnostic test implemented for *Kepler* has not been ported for TESS. Difference image centroid offsets computed in DV have proven to be far more useful for identifying TCEs due to background sources in TESS.

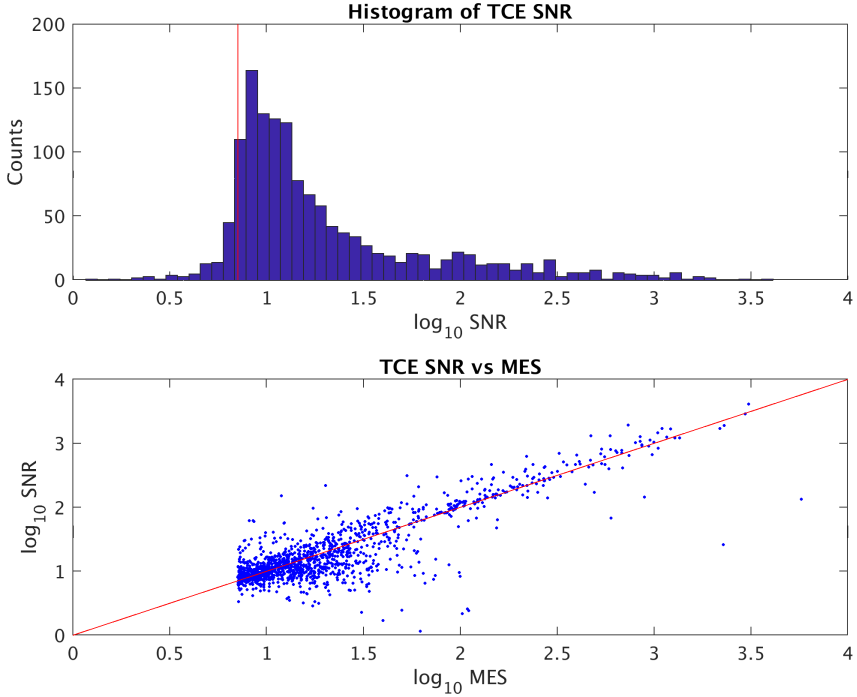


Figure 11: Top: Histogram of limb-darkened transiting planet model fit signal-to noise ratios (SNRs) of 1390 TCEs with $\text{SNR} > 1\sigma$. The SNR axis is logarithmic. The solid red line marks the transit search detection threshold (7.1σ). Bottom: SNR versus MES (transit search detection statistic) for 1390 TCEs with $\text{SNR} > 1\sigma$. MES is displayed logarithmically on the x-axis and SNR is displayed logarithmically on the y-axis. The solid red line indicates $\text{SNR} = \text{MES}$.

A total of 1558 TCEs were generated for the 1031 targets that successfully completed DV. The first TCE on each target (1031) was identified in TPS proper, and the remaining TCEs (527) were identified in the multiple planet search calls to TPS from DV. The TCE breakdown by target is shown in Table 3. It should be noted that TCEs in systems with four or more are unlikely to represent viable transiting planet candidates. Rather, these TCEs are typically driven by data artifacts, short timescale stellar variability, and contact binaries with modulated light curves.

DV timed out for one target (TIC 289840926) with complex short-timescale variability; DV results and archive products are not available for this target. This target does not appear to be a credible transiting planet host. The issue that prompted this timeout was addressed prior to Sector 3 data processing.

A limb-darkened transiting planet model is fitted to the light curve for each TCE. The top panel of Figure 11 shows the model fit SNR for 1390 TCEs with $\text{SNR} > 1\sigma$, while the bottom panel shows the model fit SNR versus transit search Multiple Event Statistic (MES). For TCEs associated with transiting planets, the model fit SNR would be expected to meet or exceed the transit search detection statistic—as discussed by Twicken et al. (2016), the model fit ephemeris is more refined, the signal-template match is better, and the performance

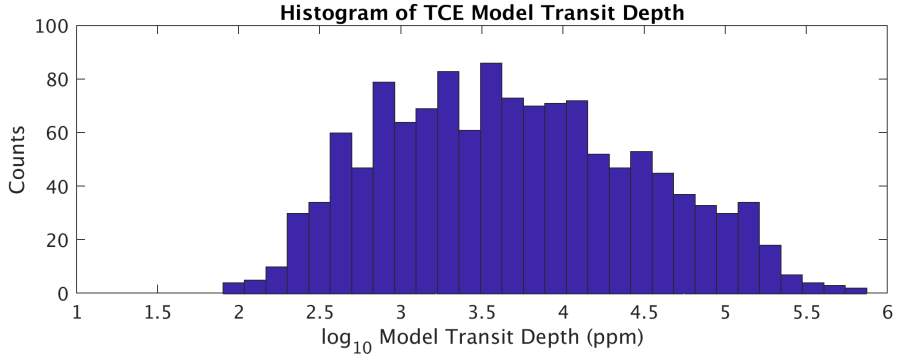


Figure 12: Histogram of limb-darkened transiting planet model transit depth for 1283 TCEs with $\text{SNR} > 7.1\sigma$. Transit depth is displayed on a logarithmic scale in units of ppm.

Table 3: Sector 1 TCE Numbers

Number of TCEs	Number of Targets	Total TCEs
1	661	661
2	266	532
3	67	201
4	24	96
5	10	50
6	3	18
—	1031	1558

of the whitener is improved because the in-transit cadences are known in advance. If the SNR does not meet or exceed the MES, the TCE may have been triggered by phenomena other than a transit or (detached) eclipse. There is a population of TCEs for which the model fit SNR does not even meet the 7.1σ detection threshold, and these TCEs should be scrutinized closely as to their planet candidate viability.

The distribution of transit depths derived from the transiting planet model fits for TCEs with $\text{SNR} > 7.1\sigma$ is displayed in the top panel of Figure 12. The model transit depths range down to the order of 100 ppm, but the bulk of the transit depths are considerably larger. DV derives planet and orbit parameters for each TCE from the limb-darkened transit model fit, including planet radius, orbit semi-major axis, equilibrium temperature, and effective stellar flux.

Along with the full DV report, a one-page DV Report Summary is produced for each TCE. An example Report Summary for an artifact driven TCE is shown in Figure 13. The report illustrates a two-transit TCE triggered by light curve artifacts in each orbit of the observing sector. This particular target was observed on Camera 1, CCD 4 in Sector 1. In total, there were three such false alarms on the same target.

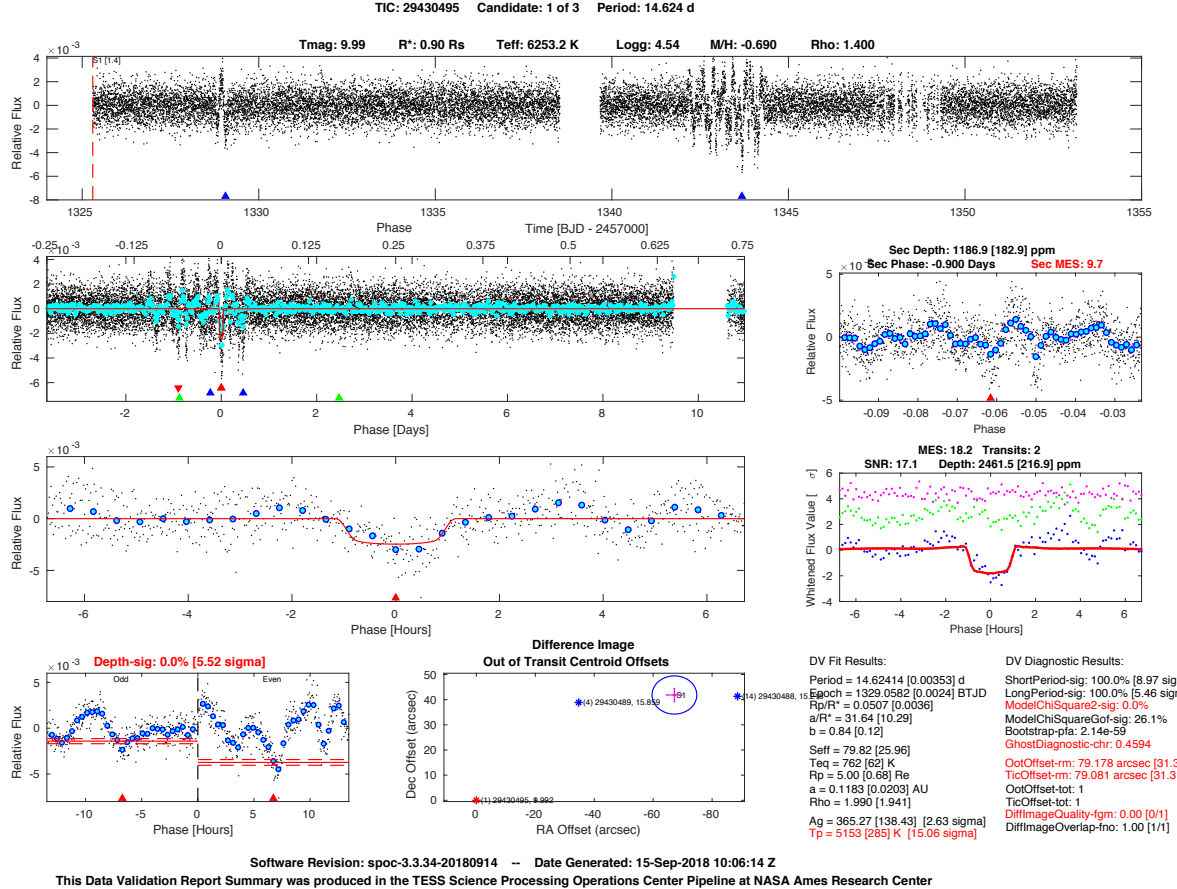


Figure 13: One-page DV report summary for TIC 29430495. This would-be 5.0 Earth radius planet with 14.6 d orbital period is clearly attributable to artifacts in each of the two Sector 1 orbits. This is the first of three such false alarms on the same host star. The two “transit” events are marked with blue triangles on the detrended light curve for this target in the upper panel.

References

- Bryson, S. T., Jenkins, J. M., Klaus, T. C., et al. 2017, Kepler Data Processing Handbook: Target and Aperture Definitions: Selecting Pixels for Kepler Downlink, Tech. rep., NASA Ames Research Center
- Christiansen, J. L., Jenkins, J. M., Caldwell, D. A., et al. 2012, *PASP*, 124, 1279
- Jenkins, J. M. 2017, Kepler Data Processing Handbook: Overview of the Science Operations Center, Tech. rep., NASA Ames Research Center
- Jenkins, J. M., Chandrasekaran, H., McCauliff, S. D., et al. 2010, in Proc. SPIE, Vol. 7740, Software and Cyberinfrastructure for Astronomy, 77400D
- Jenkins, J. M., Twicken, J. D., McCauliff, S., et al. 2016, in Proc. SPIE, Vol. 9913, Software and Cyberinfrastructure for Astronomy IV, 99133E
- Li, J., Tenenbaum, P., Twicken, J. D., et al. 2018, ArXiv e-prints, arXiv:1812.00103
- Morris, R. L., Twicken, J. D., Smith, J. C., et al. 2017, Kepler Data Processing Handbook: Photometric Analysis, Tech. rep., NASA Ames Research Center
- Ricker, G. R., Winn, J. N., Vanderspek, R., et al. 2015, Journal of Astronomical Telescopes, Instruments, and Systems, 1, 014003
- Smith, J. C., Stumpe, M. C., Van Cleve, J. E., et al. 2012, *PASP*, 124, 1000
- Stumpe, M. C., Smith, J. C., Catanzarite, J. H., et al. 2014, *PASP*, 126, 100
- Twicken, J. D., Jenkins, J. M., Seader, S. E., et al. 2016, *Astron. J.*, 152, 158
- Twicken, J. D., Catanzarite, J. H., Clarke, B. D., et al. 2018, *PASP*, 130, 064502
- Van Cleve, J. E., & Caldwell, D. A. 2016, Kepler Instrument Handbook, Tech. rep., NASA Ames Research Center
- Vanderspek, R., Doty, J., Fausnaugh, M., & Villaseñor, J. 2016, TESS Instrument Handbook, Tech. rep., Kavli Institute for Astrophysics and Space Science, Massachusetts Institute of Technology

Acronyms and Abbreviation List

BTJD Barycentric-corrected TESS Julian Date

CAL Calibration Pipeline Module

CBV Cotrending Basis Vector

CCD Charge Coupled Device

CDPP Combined Differential Photometric Precision

COA Compute Optimal Aperture Pipeline Module

CSCI Computer Software Configuration Item

CTE Charge Transfer Efficiency

Dec Declination

DR Data Release

DV Data Validation Pipeline Module

DVA Differential Velocity Aberration

FFI Full Frame Image

FIN FFI Index Number

FITS Flexible Image Transport System

FOV Field of View

FPG Focal Plane Geometry model

KDPH Kepler Data Processing Handbook

KIH Kepler Instrument Handbook

KOI Kepler Object of Interest

MAD Median Absolute Deviation

MAP Maximum A Posteriori

MAST Mikulski Archive for Space Telescopes

MES Multiple Event Statistic

NAS NASA Advanced Supercomputing Division

PA Photometric Analysis Pipeline Module

PDC Pre-Search Data Conditioning Pipeline Module

PDC-MAP Pre-Search Data Conditioning Maximum A Posteriori algorithm

PDC-msMAP Pre-Search Data Conditioning Multiscale Maximum A Posteriori algorithm

PDF Portable Document Format

POC Payload Operations Center

POU Propagation of Uncertainties

ppm Parts-per-million

PRF Pixel Response Function

RA Right Ascension

RMS Root Mean Square

SAP Simple Aperture Photometry

SDPDD Science Data Product Description Document

SNR Signal-to-Noise Ratio

SPOC Science Processing Operations Center

SVD Singular Value Decomposition

TCE Threshold Crossing Event

TESS Transiting Exoplanet Survey Satellite

TIC TESS Input Catalog

TIH TESS Instrument Handbook

TJD TESS Julian Date

TOI TESS Object of Interest

TPS Transiting Planet Search Pipeline Module

UTC Coordinated Universal Time

XML Extensible Markup Language